

PHONONIC BRAGG REFLECTORS FOR THERMAL ISOLATION OF SEMICONDUCTOR QUBITS

SEBASTIAN KOCK

Bachelor's Thesis in Physics

presented to

**The Faculty of Mathematics, Computer Science and Natural Sciences at
RWTH Aachen University**
Department of Physics, Institute II C

September 2021

supervised by

Prof. Hendrik Bluhm, Ph.D.
Tobias Hangleiter, M.Sc.

ABSTRACT

Decoupling a quantum state from its environment is a key challenge in the quest for building a quantum computer. In semiconductor qubits, the influence of influence of heat transport by phonons originating in heat transport originating in control electronics will play a significant role for the decoherence time of qubits in large scale quantum processors.

This work discusses the concept of a Bragg reflector for coherent reflection of thermal phonons in order to increase thermal isolation of semiconductor qubits. For that purpose, a numerical simulation tool is developed that can calculate the phonon transmission through such structures using the Transfer Matrix Method. All functionalities are presented with the aim of providing future scientists with an easy introduction to the use of the code. The validity of the obtained results is demonstrated by comparing the results for known configurations.

CONTENTS

1	INTRODUCTION	3
1.1	Superlattice Structures for Thermal Isolation	3
1.2	Previous Work	4
1.3	Outline	5
2	THEORY	7
2.1	Kinetic Transport Theory of Phononic Heat Conduction	7
2.2	Elastic Properties of Materials	9
2.2.1	Stress Tensor	9
2.2.2	Strain Tensor	10
2.2.3	Stress-Strain Relations	10
2.3	Elastic Waves	11
2.3.1	Solution for Isotropic Materials	12
2.3.2	Elastic Wave Scattering at an Interface	13
2.3.3	Scattering at a System of Layers	19
2.3.4	Properties of Distributed Bragg Reflectors	24
3	IMPLEMENTATION	27
3.1	Code Structure and Functionality	27
3.1.1	Algorithms and their Scope of Application	28
3.1.2	Plots and Scripts for Evaluation	31
4	SIMULATIONS	33
4.1	Scattering at a Single Interface	33
4.2	Multilayer Structures	33
5	CONCLUSION	39
	Bibliography	41
A	APPENDIX	43
A.1	Concrete Form of the Condition Matrices	43
A.2	Detailed Plots Picturing Scopes of Numerical Instabilities	43
A.3	Materials in <code>materials.py</code>	46

TODO LIST

INTRODUCTION

In recent years quantum computing technology has been of rising interest to scientists and the public. The early steps of exploiting the nature of quantum states by fabricating and controlling individual qubits are overcome [1, 2] and computational advantage of quantum processors over classical computers, has already been demonstrated in some cases [3]. With scalable concepts for many, different implementations [4–7] it is only a matter of time until quantum computers can be used commercially.

However, there are still a some hurdles to overcome before current setups are at this level. One of them is to reduce the decoherence time. It is crucial for the execution of long operations or algorithms and strongly depends on external conditions like, for example, the influence of thermal radiation consisting of photons or heat conduction from phonons or electrons[8]. In solid state qubits, heat transfer by phonons is mostly enabled by electronics connected to the chip. The reduction of the decoherence time caused from heat conduction to the qubit could be solved by an intermediate medium with very low thermal conductivity shielding the chip from thermal phonons.

1.1 SUPERLATTICE STRUCTURES FOR THERMAL ISOLATION

One possible approach to construct such a medium is a superlattice structure of alternating layers of different materials whose phononic heat conduction is minimized for coherent heat phonons. This concept exploits the properties of coherent phonons modelled as coherent elastic waves and has proven to be effective for control of heat conduction at low temperatures [9]. The underlying theory of this concept focuses on a special case of the macroscopic theory of heat conduction, where heat flow is explained as diffusive scattering of phonons between regions of different temperatures. Typically the phase of a phonon changes through scattering so that interference effects are not observable at large scale structures. This means that the described layer structures need to have thicknesses far smaller than the phonon mean free path. This case is known as ballistic regime.

Further, such superlattices are known from optics as Distributed Bragg reflectors and usually consist of layer structures with alternating refraction indices. These

are known to have so called spectral band gaps which are spectral regions where the wave is fully reflected. In optics, this structure is usually used as highly efficient reflector for electromagnetic waves from a defined angle.

In contrast to the optical case, the complete spectrum of thermal radiation for all incident angles θ and polarisation modes i is relevant for the total expected heat flow through the reflector

$$J_z = \sum_{i=\{L,TV,TH\}} \int_0^{\omega_c} \int_{\theta,\phi} \mathcal{T}_i(\omega,\theta,\phi) g_i(\omega) n_B(\omega,T) \hbar\omega c_i \cos\theta d\omega d\theta d\phi \quad (1.1)$$

which will be justified later. The integrand consists of the transmittivity function $\mathcal{T}_i(\omega,\theta,\phi)$ which is defined as proportion of transmitted intensity and can be interpreted here as transmission probability density. $g_i(\omega)n_B(\omega,T)\hbar\omega$ is the spectral energy density per unit volume of the phononic thermal radiation with Bose distribution n_B and density of states g_i . Multiplying this with the phonon velocity in z-direction $c_i \cos\theta$ yields the spectral radiance of the uppermost medium which is the emitted power per frequency and spatial angle in z-direction. The exact form of $g_i(\omega)$ and ω_c is given by the Debye model which can be applied here.

Based on the cooling power of current cryostats it is estimated that the transmitted heat flux needs to be on the order of 10 mW. Also, for any power considerations the upper temperature is assumed to be $T = 1.8\text{K}$ which is a temperature that can be achieved comfortably with current methods.

The aim of this work will be to investigate practicable reflector configurations by developing a reusable simulation of elastic wave propagation through arbitrary multilayer structures.

1.2 PREVIOUS WORK

The described aim of developing a simulation environment for elastic wave propagation through multilayer structures has been already pursued by Sebastian Miles in the scope of a HiWi project for the institute. The level of development at the time of the beginning of my project consisted of the two implementations for the later described Transfer Matrix Method and the LSE Method, which could only deliver valid results for cases without mixing of modes at an interface and also similar numerical issues that were encountered in this work. In order to avoid adopting those errors, the here described implementation was written independently.

However, a large part of the theoretical foundations of the described methods were researched and summed up in a currently not published paper by Miles. The present theoretical introduction follows it roughly and is worked out with more

detail than it is usual in a paper. All files described in the following are stored in the project repository `python-distributed_bragg_reflectors`¹

1.3 OUTLINE

In the following, the theory of phononic heat conduction in the ballistic regime is introduced with focus on explaining the solving methods used in the developed simulation tool. This requires a detailed consideration of elastic wave mechanics. Also, the simulation methods for computing the transmission through a system of layers are derived and some general properties of such structures are described. The code structure of the simulation that was written on basis of that theory is presented afterwards with the aim of providing an overview over functionalities and scope of application. Further these methods are validated for single interface scattering and its capabilities are demonstrated on an exemplary structure.

¹ https://git.rwth-aachen.de/qutech/python-distributed_bragg_reflectors

THEORY

Subsequent to the description of the aim it is useful to revisit the related concepts in more detail to justify the utilised solving methods. At the same time, a consistent notation is introduced.

Firstly, the kinetic transport theory of phononic heat conduction is considered with more care in order to justify the integral from the introduction. After that, the tensor formalism for elastic properties of rigid bodies is introduced and elastic waves are derived and analysed further. At the end, it is shown how wave propagation through multilayer structures can be calculated and also some special cases are considered. This discussion will be mostly based on [10], if not otherwise stated.

It should be noted in advance that vectors are denoted by a single underline and tensors or tensor fields of higher order by a number of underlines corresponding to their order. Also, Einstein summation convention should be applied if no explicit summation is given in the same formula.

2.1 KINETIC TRANSPORT THEORY OF PHONONIC HEAT CONDUCTION

In solids, heat is transported by both phonons and electrons. However, we consider only structures that are electrically insulating in total, so that we can model thermal heat conduction by considering only phonons.

A typical situation for analysing heat conduction requires a spatial variation of temperature. We assume this variation of temperature to be so small that in a sufficiently large spatial region with temperature T we can define the mean number of phonons $\langle n \rangle$ in frequency mode ω as

$$\langle n \rangle = n_B(\omega, T) = \frac{1}{e^{\frac{\hbar\omega}{k_B T}} - 1} \quad (2.1)$$

with reduced Planck constant \hbar and Boltzmann constant k_B .

On macroscopic scales, these phonons move through the material and scatter statistically after traveling the mean free path Λ . In general, heat transport by phonons can be described by the phonons diffusing through the material and thereby transporting energy. However, as other quasi particles they can be modelled as waves but interference effects can be only exploited, if the interfering

waves have a constant phase difference. For this reason, a structure reflecting phonons needs to be sufficiently smaller than that mean free path.

To quantify the heat transport, we can look at the heat quantity ΔQ that is transported through a reference plane with area A per time interval Δt by phonons of fixed mode ω . This energy can be calculated by multiplying the spectral phonon energy density $\frac{\epsilon(\omega, T)}{V}$ by the volume of phonons propagating through A with velocity v which results in

$$\frac{\Delta Q}{\Delta t} = \frac{\epsilon(\omega, T)}{V} A \cdot v_z . \quad (2.2)$$

The mean energy per mode is given by $\epsilon(\omega, \theta) = \hbar\omega \langle n \rangle$ neglecting ground state energy $\hbar\omega/2$, that is not relevant for heat conduction. Summing over all phonon modes \underline{k}_n and polarisations i we can calculate the total heat flux in z-direction by

$$J_z = \frac{\Delta Q}{\Delta t A} = \frac{1}{V} \sum_{\underline{k}_n, i} \hbar\omega(\underline{k}_n) n_B(\omega(\underline{k}_n), T) v_z(\underline{k}_n) . \quad (2.3)$$

As the qubits are cooled to temperatures of less than 30 mK, the temperature of the uppermost medium is also at low Kelvin temperatures. This justifies using the Debye model for the description of phonons which assumes linear dispersion $\omega(k) = c_i |k|$. In that model the phonon velocity results in $v = \frac{\partial\omega}{\partial k} = c$ and we can approximate the sum over all phonon modes \underline{k}_n in the continuum limit as an integral, resulting in

$$J_z = \sum_{i=\{L, TV, TH\}} \int_0^{\omega_c} \int_{\theta, \phi} g_i(\omega) n_B(\omega, T) \hbar\omega c_i \cos\theta d\omega d\theta d\phi . \quad (2.4)$$

The mentioned density of states per unit volume and mode takes the form of $g_i(\omega) = \frac{\omega^2}{2\pi^2 c_i^3}$ [11] which is only valid with Debye frequency $\omega_D = (6\pi^2 n c_i^3)^{1/3}$ as cutoff frequency ω_c . Here, n is the atomic density of the uppermost medium. The quantity that is calculated by carrying out the angle integration of equation 2.4 yields the spectral radiance of the upper medium.

In a setup where a multi layer structure can reflect incoming phonons, we can define the transmittivity $\mathcal{T}(\omega, \theta, \phi)$ as probability for a phonon of incident angles θ and ϕ to be transmitted through the structure. Its value can be determined from the scattered intensities as it will be discussed later. Inserting $\mathcal{T}_i(\omega, \theta, \phi)$ into the derived heat flux yields the transmitted heat flux through a reflector structure as presented in equation 1.1.

With atomic densities of order $10^{28} \frac{1}{\text{m}^3}$ and sound velocities of order $10^3 \frac{\text{m}}{\text{s}}$, the Debye frequency can be approximated to be in the order of 10^{13}s^{-1} . The spectral radiance for these frequencies at $T = 1.8 \text{ K}$ is less than a thousandth of its maximum

value, so that it is sufficient to choose a lower, not material dependent cutoff of $\omega_c = 3 \cdot 10^{12} \frac{1}{s}$.

In this frequency range the resulting wavelengths which are given by $\lambda = \frac{2\pi c}{\omega}$, are in the order of few nanometers, so that lattice properties of the materials can be neglected. Also, elastic anisotropies that may occur in crystal structures are simplified to an isotropic material with averaged properties.

2.2 ELASTIC PROPERTIES OF MATERIALS

In the following, the formalism for bulk elastic properties of materials is introduced. As only small deformations are relevant for the considerations in this thesis, they are assumed to be in the regime of linear elastic behaviour, thus neglecting plastic or nonlinear behaviour.

In one dimension linear elastic behaviour can be described simply by Hooke's law, which states that a small displacement Δl caused by a force F is proportional to the force. Considering an object of length l and cross-sectional area A , **stress** and **strain** can be defined as

$$\text{Stress} \quad \sigma := \frac{F}{A} \quad \quad \text{Strain} \quad \epsilon := \frac{\Delta l}{l} . \quad (2.5)$$

Hooke's law can now be reformulated as

$$\sigma = C \epsilon \quad (2.6)$$

with **Young's Modulus C** as proportional constant.

2.2.1 Stress Tensor

For objects of finite size, stress can be defined locally on infinitesimal, cubic volume elements. These volume elements get deformed by forces that are applied to the object. If we consider a general force $\Delta \underline{F}$ acting on a surface element ΔA we can always divide this force into a normal component $\Delta \underline{F}_n$ and two mutually perpendicular tangential components $\Delta \underline{F}_{t1}$ and $\Delta \underline{F}_{t2}$. This implies the general definition of the stress tensor as

$$\sigma_{ij} = \frac{\text{force in direction i}}{\text{surface with normal in direction j}} . \quad (2.7)$$

where indices i and j denote one of the spatial directions x, y or z . If we assume the volume element to be in equilibrium, it follows that the normal forces

on opposite sites and tangential forces on neighbouring sides equal each other. The latter implies that $\sigma_{ij} = \sigma_{ji}$. This leaves 6 independent components, the three normal stresses σ_{ii} and the three shear stresses σ_{ij} .

2.2.2 Strain Tensor

Deformation of a three-dimensional object can be described using the displacement field $\underline{u}(\underline{r}) := \underline{r}'(\underline{r}) - \underline{r}$, which defines a displacement vector for each point \underline{r} in space in comparison to the deformed position \underline{r}' . Local stress only relates to change in displacement relative to neighbouring positions which allows to consider the Taylor expansion in first order

$$\underline{u}(\underline{r} + \Delta \underline{r}) = \underline{u}(\underline{r}) + \underline{\nabla} \underline{u}(\underline{r}) \Delta \underline{r} \quad (2.8)$$

with the Jacobian matrix $(\underline{\nabla} \underline{u})_{ij} = \frac{\partial u_i}{\partial r_j}$. This in turn can be decomposed into a symmetric part and an antisymmetric part. The symmetric part is defined as strain tensor:

$$\epsilon_{ij} = \frac{1}{2} \left(\frac{\partial u_i}{\partial r_j} + \frac{\partial u_j}{\partial r_i} \right) \quad (2.9)$$

It is a dimensionless measure for local deformation in contrast to the antisymmetric part, which represents local rotation of the unit volume that does not cause tension.

2.2.3 Stress-Strain Relations

Having introduced the stress and the strain tensors, equation 2.6 can be generalised to three dimensions, thereby taking anisotropies of the material into account:

$$\sigma_{ij} = C_{ijkl} \epsilon_{kl} \quad \text{or} \quad \underline{\underline{\sigma}} = \underline{\underline{C}} \cdot \underline{\underline{\epsilon}} \quad (2.10)$$

This defines the **Elasticity tensor** as order 4 tensor with unit force / area. In general this tensor contains 81 components. However, both the stress

and the strain tensor are symmetric, so that $C_{ijkl} = C_{jikl} = C_{ijlk}$. This reduces the number of independent components to 36 and makes it possible to describe the Elasticity tensor as a 6×6 matrix. For this representation, the so called Voigt notation maps pairs of coefficients of elasticity, strain and stress tensor to a single index as in table 2.1 This simplifies the notation of elasticity significantly, but it should be treated carefully. Tensors written in Voigt notation do not transform like vectors in each index.

$$xx \rightarrow 1 \quad yy \rightarrow 2 \quad zz \rightarrow 3 \quad yz = zy \rightarrow 4 \quad xz = zx \rightarrow 5 \quad xy = yx \rightarrow 6$$

Table 2.1: Voigt notation

One can also prove that $C_{ijkl} = C_{klij}$ considering elastic energy (see section 4.3.1 of [10]) which leads to 21 independent components. Further simplifications derive from crystal symmetry or limitations in anisotropy. In the following treatment, the material is assumed to be isotropic, which reduces the number of independent components to 2. These are typically introduced as Lamé constants λ and μ defined by the relation

$$\sigma_{ij} = \lambda \delta_{ij} \epsilon_{kk} + 2\mu \epsilon_{ij} , \quad (2.11)$$

which derives from equation 2.10 by regarding isotropy of the material [12]. From this equation the elasticity tensor can be expressed by a simplified 6×6 matrix as in:

$$\underline{\underline{\sigma}} = \underline{\underline{C}} \cdot \underline{\underline{\epsilon}} = \begin{pmatrix} \lambda + 2\mu & \lambda & \lambda & 0 & 0 & 0 \\ \lambda & \lambda + 2\mu & \lambda & 0 & 0 & 0 \\ \lambda & \lambda & \lambda + 2\mu & 0 & 0 & 0 \\ 0 & 0 & 0 & 2\mu & 0 & 0 \\ 0 & 0 & 0 & 0 & 2\mu & 0 \\ 0 & 0 & 0 & 0 & 0 & 2\mu \end{pmatrix} \cdot \begin{pmatrix} \epsilon_1 \\ \epsilon_2 \\ \epsilon_3 \\ \epsilon_4 \\ \epsilon_5 \\ \epsilon_6 \end{pmatrix} . \quad (2.12)$$

2.3 ELASTIC WAVES

This formalism can now be used to introduce elastic waves. Their existence and behaviour depends on the equations of motion of the regarded medium. To obtain these, we consider at first a small volume $\Delta V = \Delta x \Delta y \Delta z$ that is subject to a stress $\sigma_{xx}(x)$ on the one side and to $\sigma_{xx}(x + \Delta x)$ on the other side. The resulting net force becomes thus

$$\Delta F_x = [\sigma_{xx}(x + \Delta x) - \sigma_{xx}(x)] \Delta z \Delta y = \frac{\partial \sigma_{xx}}{\partial x} \Delta x \Delta y \Delta z \quad (2.13)$$

by approximating $\sigma_{xx}(x + \Delta x)$ in first order and setting the frame of reference to the center of mass of the volume. The force leads to a displacement u_x of the volume in x direction and equals the product of the mass $\rho \Delta x \Delta y \Delta z$ and acceleration in x direction $\frac{\partial^2 u_x}{\partial t^2}$. This yields the one dimensional partial differential equation

$$\rho \frac{\partial^2 u_x}{\partial t^2} = \frac{\partial \sigma_{xx}}{\partial x} \quad (2.14)$$

Assuming an isotropic material and using relation 2.10, we get

$$\rho \frac{\partial^2 u_x}{\partial t^2} = C_{11} \frac{\partial \epsilon_{xx}}{\partial x} = C_{11} \frac{\partial^2 u_x}{\partial x^2} \quad (2.15)$$

In an anisotropic medium the other stress components need to be taken into account leading to the general wave equation

$$\rho \frac{\partial^2 u_i}{\partial t^2} = \frac{\partial \sigma_{ij}}{\partial x_j} = C_{ijkl} \frac{\partial^2 u_l}{\partial x_j \partial x_k} \quad (2.16)$$

2.3.1 Solution for Isotropic Materials

In the following analysis, only isotropic media will be considered. In this case the isotropic stress-strain relation, equation 2.12, can be inserted in the wave equation which yields

$$\rho \frac{\partial^2 \underline{u}}{\partial t^2} = (\lambda + \mu) \underline{\nabla}(\underline{\nabla} \cdot \underline{u}) + \mu \underline{\nabla}^2 \underline{u} \quad (2.17)$$

By using the relation $\underline{\nabla}^2 \underline{u} = \underline{\nabla}(\underline{\nabla} \cdot \underline{u}) - \underline{\nabla} \times (\underline{\nabla} \times \underline{u})$ for the vector Laplace operator one can express it as

$$\rho \frac{\partial^2 \underline{u}}{\partial t^2} = (\lambda + 2\mu) \underline{\nabla}(\underline{\nabla} \cdot \underline{u}) - \mu \underline{\nabla} \times (\underline{\nabla} \times \underline{u}) \quad (2.18)$$

If we now consider the Helmholtz decomposition of the displacement fields

$$\underline{u} = \underline{\nabla} \Phi + \underline{\nabla} \times \underline{\Psi} \quad (2.19)$$

with elastic potentials Φ and Ψ and insert it into 2.18, it decouples to the two equations (see [13])

$$\frac{\partial^2 \Phi}{\partial t^2} = c_L^2 \underline{\nabla}^2 \Phi, \quad (2.20)$$

$$\frac{\partial^2 \underline{\Psi}}{\partial t^2} = c_T^2 \underline{\nabla}^2 \underline{\Psi}, \quad (2.21)$$

$$\text{with } c_L = \left(\frac{\lambda + 2\mu}{\rho} \right)^{1/2} \quad \text{and} \quad c_T = \left(\frac{\mu}{\rho} \right)^{1/2}. \quad (2.22)$$

Those equations represent four wave equations for the elastic potentials with phase velocities c_L and c_T .

In analogy to electromagnetic waves we can now make the harmonic plane wave ansatz $\Phi(\underline{x}, t) = u_L e^{i(\underline{k}_L \underline{x} - \omega t)}$ and $\underline{\Psi}(\underline{x}, t) = \underline{u}_T e^{i(\underline{k}_T \underline{x} - \omega t)}$ with arbitrary amplitudes

$u_L \in \mathbb{C}$ and $\underline{u}_T \in \mathbb{C}^3$. Here, the vector $\underline{k} = \frac{2\pi}{\lambda}$ denotes the wave vector defined by the wavelength λ and ω is the circular frequency defined by the oscillation frequency f with $\omega = 2\pi f$. The differentiation between \underline{k}_L and \underline{k}_T is necessary because of the different phase velocities for the elastic potentials resulting in different wave numbers according to $c = \frac{\omega}{|\underline{k}|}$.

Substituting the wave ansätze into equation 2.19, we get

$$\underline{u} = u_L \underline{k} e^{i(\underline{k}_L \underline{x} - \omega t)} + \underline{k} \times \underline{u}_T e^{i(\underline{k}_T \underline{x} - \omega t)} \quad (2.23)$$

Here we can see now that the elastic potential Φ is responsible for waves with longitudinal polarisation and Ψ for waves with transversal propagation. Furthermore we can identify an orthonormal polarisation basis depending on the propagation direction $\hat{\underline{k}} = \frac{\underline{k}}{|\underline{k}|}$ so that \underline{u} decomposes to

$$\underline{u} = a_L \underline{p}_L e^{i(\underline{k}_L \underline{x} - \omega t)} + (a_{TH} \underline{p}_{TH} + a_{TV} \underline{p}_{TV}) e^{i(\underline{k}_T \underline{x} - \omega t)} \quad (2.24)$$

In general, the polarisation vector for longitudinal polarisation \underline{p}_L is fixed to be $\hat{\underline{k}}$. If scattering at an interface is considered, a plane of incidence can be defined that is spanned by $\hat{\underline{k}}$ and the normal vector of the interface. The transversal polarisation vectors are then defined as transversal horizontal polarisation \underline{p}_{TH} pointing out of the plane of incidence and transversal vertical polarisation \underline{p}_{TV} lying in plane of incidence orthonormal to $\hat{\underline{k}}$, here now defined as $\underline{p}_{TV} = \underline{p}_L \times \underline{p}_{TH}$. This arrangement is also shown in a 3D coordinate system in figure

To sum up, those polarisation vectors define three polarisation modes L, TH and TV denoting longitudinal, transversal horizontal and transversal vertical polarisation which can be superimposed arbitrarily. The coefficients a_i may be complex to express an additional phase between the components. However, it should be noted that this is merely convenient for calculation and that the physical wave behaves like the real part of the shown equations.

2.3.2 Elastic Wave Scattering at an Interface

Boundary Conditions

On the way to describe wave propagation through complex layer structures it is useful to consider a single interface first. In the upper half space S_1 and lower half space S_2 we assume homogeneous materials with different elastic constants and thus different sound velocities. At the interface, which is chosen to be the xy-plane the elastic properties are discontinuous. However, we can assume that

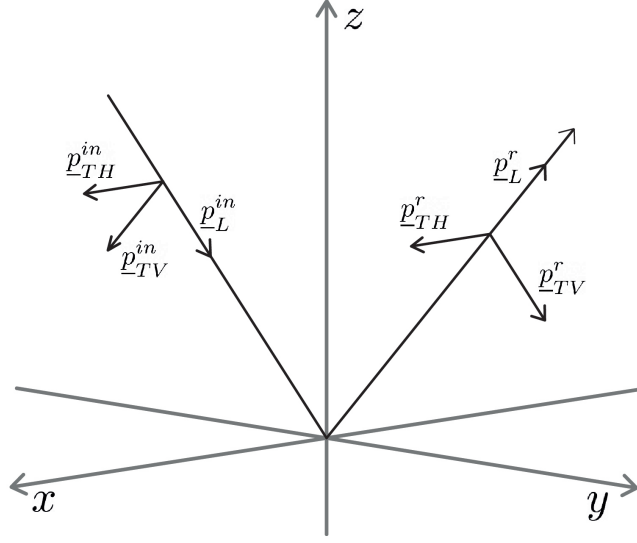


Figure 2.1: Polarisation vectors of a wave reflected at xy-plane. The different angles of the reflected modes are simplified to one angle for convenience. Both \underline{p}_L lie in the xz-plane as considered in section 2.3.2.

those layers connected strongly so that the displacement field and normal stresses are continuous at the boundary [14, pp. 182, 185]. This leads to the boundary conditions:

$$\underline{u}^{(1)}(\underline{r}, t)|_{\underline{r} \in \partial S_1} = \underline{u}^{(2)}(\underline{r}, t)|_{\underline{r} \in \partial S_2} , \quad (2.25)$$

$$\sigma_{13}^{(1)}(\underline{r}, t)|_{\underline{r} \in \partial S_1} = \sigma_{13}^{(2)}(\underline{r}, t)|_{\underline{r} \in \partial S_2} , \quad (2.26)$$

$$\sigma_{23}^{(1)}(\underline{r}, t)|_{\underline{r} \in \partial S_1} = \sigma_{23}^{(2)}(\underline{r}, t)|_{\underline{r} \in \partial S_2} , \quad (2.27)$$

$$\sigma_{33}^{(1)}(\underline{r}, t)|_{\underline{r} \in \partial S_1} = \sigma_{33}^{(2)}(\underline{r}, t)|_{\underline{r} \in \partial S_2} . \quad (2.28)$$

In these six equations displacement and stress from upper and lower medium are differentiated by the given superscript index.

Law of Refraction

If we now consider a plane wave that is incident on that interface, we can define a plane of incidence as in section 2.3.1 and rotate the coordinate system so that it equals the yz-plane which simplifies the polarisation basis. This leaves the physical problem only invariant, if we assume an isotropic material as stated

before. In that setting, the wave vector \underline{k}_i for a particular mode $i \in \{L, TV, TH\}$ can be parametrised by the angle of incidence θ as

$$\underline{k}_i = \frac{\omega}{c_i} (0, \sin(\theta_i), -\cos(\theta_i))^T. \quad (2.29)$$

The polarisation basis is then defined as

$$\underline{p}_L = \hat{k} = (0, \sin(\theta_L), -\cos(\theta_L))^T, \quad (2.30)$$

$$\underline{p}_{TH} = (1, 0, 0)^T, \quad (2.31)$$

$$\underline{p}_{TV} = \hat{k} \times \underline{p}_{TH} = (0, -\cos(\theta_{TH}), -\sin(\theta_{TH}))^T. \quad (2.32)$$

It should be noted, that despite the simplified representation in figure 2.1, the polarisation basis is not necessarily orthonormal because transversal and longitudinal angles can be different. It is now possible to extract a law of refraction from the boundary conditions in equation 2.25 (see [14, 168ff]). A simple approach is to consider scattering of the transversal horizontal mode (TH) so that the displacement is only in x-direction. An incoming plane wave with wave vector \underline{k}_{in} is partially reflected to a wave along \underline{k}_r and partially transmitted through the interface to a wave with \underline{k}_t . Also, different frequencies ω_i are assumed for the scattered waves so that the wave in the upper medium is

$$u_1^{(1)} = a_{in} e^{i(k_{in} \sin \theta_{in} y - \omega_{in} t)} + a_r e^{i(k_r (\sin \theta_r y - \omega_r t))}. \quad (2.33)$$

and in the lower medium

$$u_1^{(2)} = a_t e^{i((k_t \sin \theta_t y - \omega_t t))}. \quad (2.34)$$

Here it was used that the interface is at $z = 0$ which simplifies the following derivation. According to the boundary conditions, these displacements must equal each other at any time and for all points on the interface. This leads to the immediate conclusion that

$$\omega = \omega_{in} = \omega_r = \omega_t. \quad (2.35)$$

After removing the common factor $e^{-i\omega t}$ from the equation and expressing the wave numbers by frequency and sound velocity as $k = \frac{\omega}{c}$, we get

$$a_{in} e^{i \frac{\omega}{c_{T,1}} \sin \theta_{in} y} + a_r e^{i \frac{\omega}{c_{T,1}} \sin \theta_r y} = a_t e^{i \frac{\omega}{c_{T,2}} \sin \theta_t y}. \quad (2.36)$$

This however can be only fulfilled for all $y \in \mathbb{R}$ if the relations

$$a_{in} + a_r = a_t, \quad (2.37)$$

$$\frac{\sin \theta_{in}}{c_{T,1}} = \frac{\sin \theta_r}{c_{T,1}} = \frac{\sin \theta_t}{c_{T,2}}. \quad (2.38)$$

are met. Equation 2.38 can be also interpreted as the equality of the wave vector component parallel to the interface $k_y = \sin \theta_i \frac{\omega}{c_i}$.

The same procedure can be applied to the y and z component of the displacement field, where transversal vertical (TV) and longitudinal (L) modes need to be considered [14, p. 185]. However, one significant difference is that even for a single incident mode, both L and TV mode are possible after being reflected or transmitted. This will only add a term of the form $a_i e^{i \frac{\omega}{c} \sin \theta_i y}$ to each side of equation 2.36, but will result in analogous relations to 2.35 and 2.38, namely the invariance of frequency ω and k_2 of each mode under scattering at the interface.

To conclude, the angle θ_{out} of any outgoing polarisation mode can be determined from the incoming wave's angle θ_{in} and the sound velocities for incoming and outgoing wave c_{in}, c_{out} by

$$\frac{\sin \theta_{in}}{c_{in}} = \frac{\sin \theta_{out}}{c_{out}}. \quad (2.39)$$

This can be transferred to the optical law of snellius by introducing an effective refraction index $n_i = \frac{1}{c_i}$. Consequently, TH-polarised waves scatter like electromagnetic waves and for example the reflected angle is always the incident angle. The main difference to optics becomes clear for L and TV polarised waves. Scattering within the same polarisation mode is the same as for the TH mode, but now those modes can scatter into each other. Equation 2.39 still applies, but energy is also emitted to additional modes as shown in figure 2.2.

It is also possible to get the analytical solutions for refraction of a single mode at an interface by evaluating the remaining boundary conditions and the results from continuity of displacement. The results are usually expressed by defining a reflection coefficient r_i and a transmission coefficient t_i for participating mode $i \in \{L, TH, TV\}$ as

$$r_i := \frac{a_{r,i}}{a_{in,i}}, \quad (2.40)$$

$$t_i := \frac{a_{t,i}}{a_{in,i}}. \quad (2.41)$$

which usually have a functional dependency on the incident angle. With introducing the impedance $Z(\theta)$ of mode i of a medium as

$$Z_i(\theta) = \frac{\rho c_i}{\cos \theta}, \quad (2.42)$$

it is possible to obtain the simple relations

$$r_{TH} = \frac{Z_{in,TH} - Z_{out,TH}}{Z_{in,TH} + Z_{out,TH}}, \quad (2.43)$$

$$t_{TH} = \frac{2Z_{in,TH}}{Z_{in,TH} + Z_{out,TH}} \quad (2.44)$$

describing the refraction of TH polarisation from analogous calculations with electromagnetic waves [15, pp. 46, 14]. Analytic solutions for the remaining modes are much more complex and can be looked up in [16, p. 83].

Total Internal Reflection

Total internal reflection is known as the phenomenon when a wave is totally reflected at a boundary for incident angles greater than a critical angle θ_{tot} . If c_1 and c_2 are the phase velocities first and second medium, the outgoing angle

$$\theta_2 = \arcsin\left(\frac{c_2}{c_1} \sin(\theta_1)\right) \quad c_2 > c_1 \quad (2.45)$$

has no real solution for $\theta_1 > \theta_{tot} = \arcsin \frac{c_1}{c_2}$. There is however a complex solution and this resulting complex angle can be interpreted in the given wave formalism [15, p. 5]. This interpretation also allows to extend the concept to two arbitrary polarisation modes that the wave can scatter inbetween, regardless of propagation direction.

Considering the case $\theta_1 > \theta_{tot}$, θ_2 can be expressed as $\theta_2 = \frac{\pi}{2} + i\alpha$, $\alpha \in \mathbb{R}$. Inserting this into the general wave solution equation 2.24, we need to calculate the wave vector \underline{k} as in equation 2.29. This results in

$$k_y = k \sin \theta_2 = k \cosh \alpha, \quad k_z = k \cos \theta = ik \sinh \alpha. \quad (2.46)$$

This complex wave vector inserted into the factor $e^{ik_z z}$ yields $e^{-k \sinh \alpha z}$ which represents an evanescent wave. This type of wave is attenuated exponentially so that the wave behaves as expected.

In case of frustrated total internal reflection this exponential behaviour becomes relevant, when another interface is close to the first reflecting interface. Then it is possible for the usually totally reflected mode to transmit intensity into a mode of the third medium.

Conservation of Energy

Since acoustic waves transport energy, we can define an intensity for them and consider the conservation of energy at an interface. According to [14, p. 166] the

transmitted time averaged power per unit area of a transversal elastic wave in a homogeneous medium is

$$I_L = \frac{1}{2}(\lambda + 2\mu)\frac{\omega^2}{c_L}|a_L|^2 \quad (2.47)$$

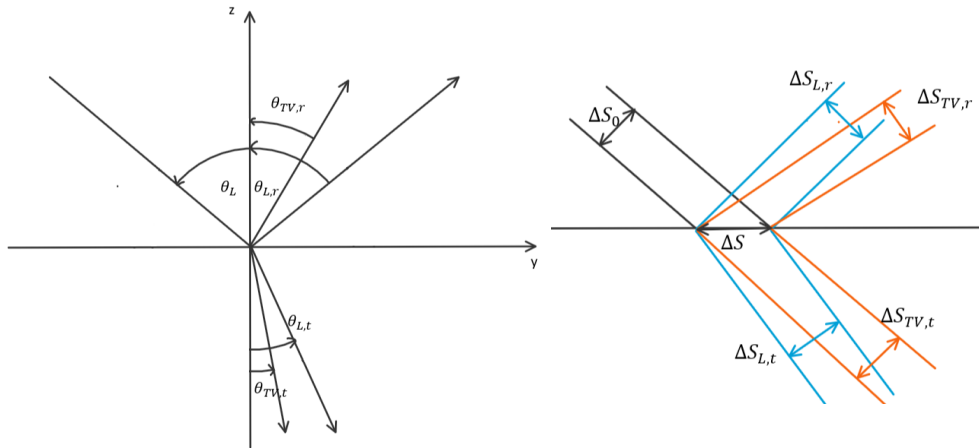
and similarly for a transversal elastic wave of a single polarisation mode

$$I_T = \frac{1}{2}\mu\frac{\omega^2}{c_T}|a_T|^2, \quad (2.48)$$

where a_T is either a_{TV} or a_{TH} depending on the regarded mode. This quantity is also known as time averaged intensity. By using the definition of c_L and c_T from equation 2.22 we get the more general relation

$$I_p = \frac{\rho\omega^2}{2}|a_p|^2 c_p \quad (2.49)$$

with $p \in \{L, TH, TV\}$ denoting the polarisation mode. It should be noted that the referred unit area is perpendicular to the direction of propagation.



(a) Refraction of a Longitudinal Elastic Wave (b) Conservation of Energy at Surface Element ΔS for an TV polarized beam

Figure 2.2

In the setting of an arbitrary polarised wave scattered at an interface, there are six possible outgoing modes as discussed previously. To get an energy relation between the intensities of each participating mode we consider the energy balance of a surface element ΔS of the interface, on which an arbitrarily polarised beam with cross-sectional area ΔS_0 and intensity I_{in} is incident. The cross-sectional

areas of the outgoing beams are named according to figure 2.2b which can be also transferred to the case of an incident TH polarised wave.

The power each beam transmits or emits is given by the product $P_p = I_p \Delta S_p$. ΔS_p is related to ΔS by $\Delta S_p = \cos \theta_p \Delta S$, p denoting any of the depicted beams and θ_p being the according angle.

In conclusion, the energy balance results in

$$I_{in} \cos \theta_{in} = \sum_{i=L,TH,TV} I_{i,r} \cos \theta_{i,r} + I_{i,t} \cos \theta_{i,t}. \quad (2.50)$$

From that we can divide by $I_{in} \cos \theta_{in}$ and define reflectivity \mathcal{R} and transmittivity \mathcal{T} of the interface as fraction of reflected and transmitted power by

$$\mathcal{R} := \frac{I_{L,r} \cos \theta_{L,r} + I_{TH,r} \cos \theta_{T,r} + I_{TV,r} \cos \theta_{T,r}}{I_{in} \cos \theta_{in}}, \quad (2.51)$$

$$\mathcal{T} := \frac{I_{L,t} \cos \theta_{L,t} + I_{TH,t} \cos \theta_{T,t} + I_{TV,t} \cos \theta_{T,t}}{I_{in} \cos \theta_{in}} \quad (2.52)$$

so that $\mathcal{R} + \mathcal{T} = 1$ is fulfilled.

This can be easily extended to multi layer structures replacing the single interface by the multi layer system so that the transmitted intensities are the intensities that propagated through the whole structure.

The relation $\mathcal{T} + \mathcal{R} = 1$ can then be used to verify the obtained results for any layer structure.

2.3.3 Scattering at a System of Layers

The considerations of one interface can now be extended to a system of N interfaces as shown in figure 2.3. Each layer gets an index n starting from the uppermost layer of index $n = 0$. The first interface from the top is still located at $z_1 = 0$ and has index $n = 1$. The subsequent interfaces follow below at depths z_n . Their depth depends on the intermediate layer thicknesses $d_n = z_n - z_{n+1}$ with layer index n . Similar as before, we assume now the displacement field in each layer n as

$$\underline{u}^{(n)}(\underline{x}, t) = \sum_{i \in \{L, TH, TV\}} t_{n,i} \underline{p}_{n,i}^t e^{i(\underline{k}_{n,i}^t \underline{x} - \omega t)} + r_{n,i} \underline{p}_{n,i}^r e^{i(\underline{k}_{n,i}^r \underline{x} - \omega t)}. \quad (2.53)$$

This formula is a superposition of a down going wave with quantities denoted by t and a upgoing wave caused by reflections with quantities denoted by r . The upgoing \underline{k}^r is flipped in z -direction compared to \underline{k}^t . Further, the complex amplitudes of down and upgoing modes are directly denoted by $t_{n,i}$ and $r_{n,i}$. As the angle $\theta_{n,i}$

between \underline{k} and z-axis is changes by scattering, also $\underline{k}_{n,i}$ and polarisation vector $\underline{p}_{n,i}$ is different for each material.

To evaluate the transmission through the stack of layers, it is the task is now to calculate the coefficients $t_{N,i}$ and $r_{1,i}$ given coefficients $t_{1,i}$ and with the assumption $r_{N,i} = 0$ for all $i \in \{L, TH, TV\}$. This assumption can be made because we only consider the incoming power on the chip. Thermal radiation from the chip itself is significantly lower. We further choose exactly one $t_{1,i} = 1$ to mark the incident mode. This simplifies solving the problem and lets the coefficients $t_{N,i}$ and $r_{1,i}$ become the transmission and reflection coefficients of the layer system.

For this, all $6N$ boundary conditions need to be solved. These are constructed by inserting the general displacement field of each participating layer as in equation 2.53 in the boundary conditions for a single interface (equation 2.25). As a result each displacement field of an enclosed layer is evaluated twice, once at the upper boundary and once at the lower boundary. This results in a phase shift of $e^{-ik_z d_n}$ between upper and lower displacement.

As many systems of equations this problem can be formulated with matrices. In the following, two solution methods are introduced. In the later course, both methods will be compared to each other on the base of practical advantages and disadvantages.

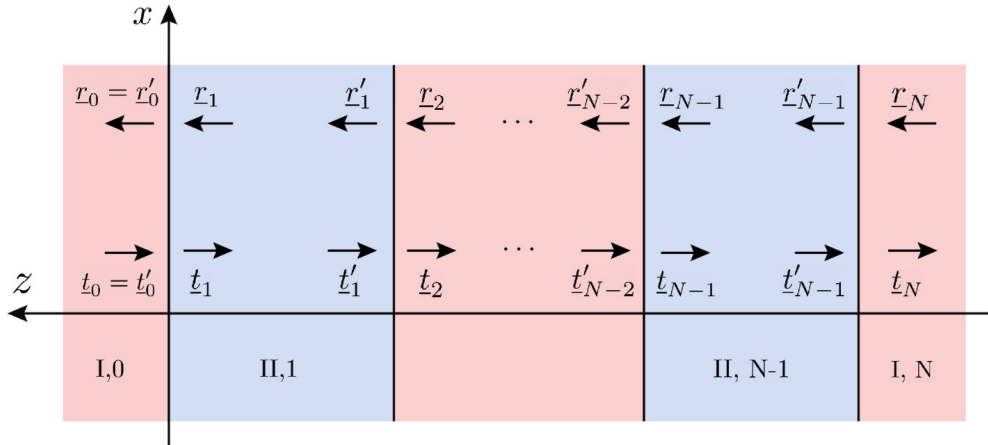


Figure 2.3: Geometry and amplitude nomenclature of a N layer strong bragg reflector

Transfer Matrix Method

To introduce the matrix formalism of the Transfer Matrix Method (TMM) it is useful to focus on a single interface with index n between layers $n-1$ and n located at depth z_n . We can define a generalised state vector \underline{v}_i in each layer i as [17]

$$\underline{v}_i = (u_1^{(i)}, u_2^{(i)}, u_3^{(i)}, \sigma_{13}^{(i)}, \sigma_{23}^{(i)}, \sigma_{33}^{(i)})^T. \quad (2.54)$$

Each of the components depends on location \underline{x} and time t in the layer. We also introduce the superscript "+" for evaluating an arbitrary multidimensional function of space and layer index n at interface \mathcal{F}_n and superscript "-" for evaluating at \mathcal{F}_{n-1} so that the boundary conditions at the n -th interface \mathcal{F}_n are

$$\underline{v}_n^+ = \underline{v}_{n+1}^-. \quad (2.55)$$

In addition to equation 2.53, the stress components in \underline{v} can be evaluated as well. From stress strain relation 2.10 we get for an isotropic material

$$C_{1313}^{(n)} \epsilon_{13}^{(n),+} = C_{1313}^{(n+1)} \epsilon_{13}^{(n+1),-}, \quad (2.56)$$

$$C_{2323}^{(n)} \epsilon_{23}^{(n),+} = C_{2323}^{(n+1)} \epsilon_{23}^{(n+1),-}, \quad (2.57)$$

$$\sum_{i=1}^3 C_{33ii}^{(n)} \epsilon_{ii}^{(n),+} = \sum_{i=1}^3 C_{33ii}^{(n+1)} \epsilon_{ii}^{(n+1),-}. \quad (2.58)$$

Furthermore, the strain can be evaluated by inserting the general displacement field 2.53 into its definition $\epsilon_{ij} = \frac{1}{2} \left(\frac{\partial u_i}{\partial r_j} + \frac{\partial u_j}{\partial r_i} \right)$.

At this point it is necessary to know all angles at which the different modes propagate through each layer in order to construct the equations as linear relations. These can be obtained by following the considerations of section 2.3.2. Because of our limitation to one incident mode on the top layer, also only one propagation angle per distinct phase velocity in the medium is possible. From the structure of $\underline{u}^{(n)}$ it is possible to construct a 6×6 matrix M_n so that

$$\underline{v}_n(z) = \underline{\underline{M}}_n \underline{\underline{P}}_n(z - z_n) \underline{a}_n. \quad (2.59)$$

This step is considered in detail in the appendix. The coefficient vector \underline{a}_n of layer n is defined as

$$\underline{a}_n = (\underline{t}_n, \underline{r}_n)^T = (t_{n,L}, t_{n,TH}, t_{n,TV}, r_{n,L}, r_{n,TH}, r_{n,TV})^T \quad (2.60)$$

containing the wave amplitudes at the upper edge of each layer $z = z_n$. As an exception, $r_{0,i}$ and $t_{0,i}$ are defined directly at the first interface.

$\underline{\underline{P}}_n(z)$ represents the phase factors due to wave propagation as diagonal matrix

$$\underline{\underline{P}}_n(z) = \text{diag}\{e^{ik_{z,n}^{(L)}z}, e^{ik_{z,n}^{(TH)}z}, e^{ik_{z,n}^{(TV)}z}, e^{-ik_{z,n}^{(L)}z}, e^{-ik_{z,n}^{(TH)}z}, e^{-ik_{z,n}^{(TV)}z}\}. \quad (2.61)$$

The factor $e^{k_{y,n}^{(i)}y}$ was removed from the expression as it does not change at the boundary. This automatically sets the phase of the displacement wave to zero at the upper boundary of the layer. The coefficients at the lower boundary are in the following denoted by $\underline{a}'_n = \underline{\underline{P}}_n(-d_n) \underline{a}_n$.

As a result the boundary conditions at an individual interface between layers $n-1$ and n can be written as

$$\underline{\underline{M}}_{n-1} \underline{a}'_{n-1} = \underline{\underline{M}}_n \underline{a}_n. \quad (2.62)$$

If we invert $\underline{\underline{M}}_n$, we can define the transfer matrix S_n by

$$\underline{a}_n = \underline{\underline{M}}_n^{-1} \underline{\underline{M}}_{n-1} \underline{a}'_{n-1} = \underline{S}_n \underline{a}'_n, \quad (2.63)$$

which enables us to obtain the wave coefficients after scattering by a simple matrix multiplication. Here, $\underline{\underline{M}}_n^{-1}$ must be defined as we know, that there exists a physical solution.

With this knowledge we can assemble a global transfer matrix for all interfaces by

$$\underline{S} = \underline{S}_N \cdot \underline{\underline{P}}_N(z_N - z_{N-1}) \cdot \underline{S}_{N-1} \cdot \underline{\underline{P}}_{N-1}(z_{N-1} - z_{N-2}) \cdots \underline{S}_2 \cdot \underline{\underline{P}}_2(z_2 - z_1) \cdot \underline{S}_1 \quad (2.64)$$

so that the final wave coefficients \underline{a}_N below the lowest interface are

$$\begin{pmatrix} \underline{t}_n \\ \underline{r}_n \end{pmatrix} = \underline{S} \cdot \begin{pmatrix} \underline{t}_1 \\ \underline{r}_1 \end{pmatrix} = \begin{pmatrix} \underline{T} & \underline{C}_1 \\ \underline{C}_2 & \underline{R} \end{pmatrix} \cdot \begin{pmatrix} \underline{t}_1 \\ \underline{r}_1 \end{pmatrix}. \quad (2.65)$$

Remembering that $\underline{r}_n = 0$, we can solve for \underline{r}_1 and \underline{t}_n and get

$$\underline{r}_1 = -\underline{\underline{R}}^{-1} \underline{C}_2 \underline{t}_1, \quad (2.66)$$

$$\underline{t}_n = \begin{pmatrix} \underline{T} & \underline{C}_1 \\ \underline{C}_2 & \underline{R} \end{pmatrix} \cdot \begin{pmatrix} \underline{t}_1 \\ -\underline{\underline{R}}^{-1} \underline{C}_2 \underline{t}_1 \end{pmatrix}. \quad (2.67)$$

Linear System of Equations

As an alternative, a more direct solving approach is presented by solving the system of linear equations with the inversion of a single matrix. This method will be called from now on LSE-method (Linear System of Equations).

For this method the coefficients for upgoing waves are defined to have their phase origin at the lower interface instead of the upper interface as defined in 2.61, so that the P-matrix becomes

$$\underline{\underline{P}}_n(z) = \text{diag}\{e^{ik_{z,n}^{(L)}z}, e^{ik_{z,n}^{(TH)}z}, e^{ik_{z,n}^{(TV)}z}, e^{-ik_{z,n}^{(L)}(z+d_n)}, e^{-ik_{z,n}^{(TH)}(z+d_n)}, e^{-ik_{z,n}^{(TV)}(z+d_n)}\}. \quad (2.68)$$

. The reason is that the diagonal entries evaluated at the layer boundaries $z = 0$ and $z = -d_n$ will now have always absolute values of 1 or lower. The latter is true for total internal reflection in contrary to $\underline{\underline{P}}_n$ from TMM.

For better clarity in notation we can rewrite matrix $\underline{\underline{M}}_n$ as composition of two 6×3 matrices $\underline{\underline{M}}_n = (\underline{\underline{T}}_n, \underline{\underline{R}}_n)$ and $\underline{\underline{P}}_n$ as block diagonal of two 3×3 matrices $\underline{\underline{P}}_n = \text{diag}\{\underline{\underline{D}}_n(z), \underline{\underline{D}}_n(-(z+d_n))\}$. The diagonal matrix $\underline{\underline{D}}_n$ is here defined as a 3×3 diagonal matrix with $\underline{\underline{D}}_n(z) = \text{diag}\{e^{ik_{z,n}^{(L)}z}, e^{ik_{z,n}^{(TH)}z}, e^{ik_{z,n}^{(TV)}z}\}$

The boundary conditions at interface n , below layer n are then

$$\left(\underline{\underline{T}}_n, \underline{\underline{R}}_n \cdot \underline{\underline{D}}_n(-d_n)\right) \begin{pmatrix} t_n \\ r_n \end{pmatrix} = \left(\underline{\underline{T}}_{n-1} \cdot \underline{\underline{D}}_{n-1}(-d_{n-1}), \underline{\underline{R}}_{n-1}\right) \begin{pmatrix} t_{n-1} \\ r_{n-1} \end{pmatrix}. \quad (2.69)$$

With $\underline{\underline{T}}'_{n-1} = \underline{\underline{T}}_{n-1} \cdot \underline{\underline{D}}_{n-1}(-d_{n-1})$ and analogously for $\underline{\underline{R}}'_n$, this is equivalent to

$$\left(\underline{\underline{T}}'_{n-1}, \underline{\underline{R}}_{n-1} - \underline{\underline{T}}_n, -\underline{\underline{R}}'_n\right) \begin{pmatrix} t_{n-1} \\ r_{n-1} \\ t_n \\ r_n \end{pmatrix} = 0. \quad (2.70)$$

This denotes now a 6×12 matrix for a single interface. In general the total system is constructed as $6N \times 6N$ matrix

$$\begin{pmatrix} \underline{\underline{R}}_{\underline{\underline{0}}} & -\underline{\underline{T}}_{\underline{\underline{1}}} & -\underline{\underline{R}}'_{\underline{\underline{1}}} & 0 & 0 & \cdots & 0 \\ 0 & \underline{\underline{T}}'_{\underline{\underline{1}}} & \underline{\underline{R}}_{\underline{\underline{1}}} & -\underline{\underline{T}}_{\underline{\underline{2}}} & -\underline{\underline{R}}'_{\underline{\underline{2}}} & \cdots & \vdots \\ \vdots & \ddots & \ddots & \ddots & \ddots & \ddots & \vdots \\ \vdots & \ddots & \ddots & \ddots & \ddots & \ddots & \vdots \\ 0 & \cdots & \cdots & 0 & \underline{\underline{T}}'_{\underline{\underline{N-1}}} & \underline{\underline{R}}_{\underline{\underline{N-1}}} & -\underline{\underline{T}}_{\underline{\underline{N}}} \end{pmatrix} \begin{pmatrix} r_0 \\ t_1 \\ r_1 \\ \vdots \\ t_N \end{pmatrix} = \begin{pmatrix} -\underline{\underline{T}}_{\underline{\underline{0}}} t_0 \\ 0 \\ \vdots \\ \vdots \\ \underline{\underline{R}}_{\underline{\underline{N}}} r_N \end{pmatrix}. \quad (2.71)$$

The transfer of $\underline{\underline{T}}_{\underline{\underline{0}}} t_0$ and $\underline{\underline{R}}_{\underline{\underline{N}}} r_N$ is necessary to ensure quadratic shape of the matrix which is necessary for inversion. However, this limits the number of interfaces to $N > 1$. By setting $r_N = 0$ as before we obtain r_0 and t_N after inverting the $6N \times 6N$ matrix.

2.3.4 Properties of Distributed Bragg Reflectors

In case of normal incidence on the reflector, the modes L and TV do not mix and the relations of transmission and reflection become analogous to optical waves. This can be seen from 2.39 and the fact that a displacement normal to the interface does not produce a parallel displacement and the other way round. Therefore, fundamental properties of Distributed Bragg Reflectors for optical waves apply here as well.

For the following considerations, many optics based sources are reinterpreted as acoustic quantities. The already mentioned concept of impedance is also applicable to electromagnetic waves by defining it as the ratio of electric magnetic field amplitude in the medium [15]. This evaluates to

$$Z = \sqrt{\frac{\mu_0 \mu_r}{\epsilon_0 \epsilon_r}} = Z_0 \frac{\mu_r}{n}, \quad (2.72)$$

with vacuum permeability μ_0 and vacuum permittivity ϵ_0 and the relative permeability and permittivity denoted by r. Z_0 is the vacuum impedance. It is usual to assume $\mu_r = 1$ as most regarded materials are non magnetic, so that $Z = Z_0/n$ is valid. As a result, relations for optical Bragg reflectors at normal incidence can be easily converted to relations for acoustic waves under normal incidence.

The typically used DBR structure consists of a repeated unit cell of two layers with impedances $Z_{1,i}$ and $Z_{2,i}$ for different modes i . The thicknesses are often chosen to have a thickness of a quarter wavelength of a selected frequency mode to be reflected. With sufficient number of repetitions of this unit cell, spectral band gaps form, where waves with the selected frequency and a certain interval around it are reflected with high reflectivities. Moreover, the described setup within the unit cell proves to maximize the spectral gap width to mid gap frequency ratio $\frac{\Delta f}{f_0}$ [18].

In a more general setup, where the single layers do not have exactly the thickness of a quarter wavelength of a selected frequency mode, frequency stop bands will still form. This is because of the periodicity of the unit cell. For electromagnetic waves the stop bands form around the Bragg wavelength

$$m \lambda_B / 2 = n_1 d_1 + n_2 d_2 \quad m = 1, 2, 3, \dots \quad (2.73)$$

with refraction indices $n_i = \frac{c_0}{c_i}$. To get an analogous relation for elastic waves, we can simply replace the vacuum speed of light c_0 by an arbitrary sound velocity. If λ_B is then expressed as bragg frequency $f_B = \frac{c_0}{\lambda_B}$ we get a similar result with known quantities as

$$2 \frac{f_B}{m} = \left(\frac{d_1}{c_1} + \frac{d_2}{c_2} \right)^{-1} = \left(\frac{\rho_1 d_1}{Z_1} + \frac{\rho_2 d_2}{Z_2} \right)^{-1} \quad (2.74)$$

which is also valid for acoustic waves [19]. In addition to the described position of the bandgaps, also their width can be derived. It appears that the spectral gap width to bragg frequency ratio of the first bandgap can be expressed as

$$\frac{\Delta f}{f_B} = \frac{4}{\pi} \arcsin \left(\frac{|Z_1 - Z_2|}{Z_1 + Z_2} \right) \quad [18]. \quad (2.75)$$

These relations can be used to verify the obtained results from the simulation.

IMPLEMENTATION

On basis of the preceding theory a full simulation of acoustic wave propagation through multilayer structures was developed. This will be described in more detail in the following aiming to provide a short introduction into code structure and functionality. Arisen challenges and their solution will be presented afterwards.

3.1 CODE STRUCTURE AND FUNCTIONALITY

The main components of the project are represented by the three python modules `dbf.py`, `materials.py` and `plotfunctions.py` to organise written methods by purpose.

`materials.py` contains elastic parameters of materials that were considered for usage in a reflector structure. Each entry is a python function that returns density ρ and elastic constants λ and μ . Most databases accessible through the internet contain different elastic constants like Young's Modulus or Poisson's ratio, so that those are converted with help of a formula table as in [12, p. 30]. The exact materials and their sources are listed in table A.1

The file `dbf.py` contains the most important simulation tools. Those functions are structured in two classes, `Reflector` and `Layer` to reduce the number of parameters to be passed to the next method.

The main idea for the `Layer` class is to wrap the important material parameters λ , μ and ρ passed from a material parameter function and to convert them internally to sound velocities c_i and elastic tensor C_{ijkl} . In addition, each object stores its thickness and material name. The latter is useful for fast identification of the layer material and debugging outputs. Also, it contains several methods for calculation of Layer specific quantities. One of those quantities is `getConditionMatrix()` which assembles the condition matrix $\underline{\underline{M}}_n$ from equation 2.59 for a given incident angle θ and frequency ω . In the process, the layer specific wave vector \underline{k}_i is calculated by `Layer.getK()` for every mode from incident angle and frequency. The phase velocities are accessed from the object. Calculation of polarisation vectors (`getPolarisations()`) and strain tensor (`getStrain()`) follows the same principle. The functions `Intensity()` imple-

menting equation 2.49 and `getPropagationMatrix()` implementing $\underline{P}_{=n}$ from equation 2.61 support the later mentioned methods from `Reflector`.

To construct a layer structure that can be evaluated by the simulation tools of `Reflector`, those `Layer` objects can be assembled in a list, which indicates the order of Layers in the reflector structure. Together with the defined thicknesses of each `Layer` object this forms an unambiguous representation of a physical layer structure.

This list of `Layer` objects is then passed to the constructor of a `Reflector` object and stored as deep copy of the initial list to avoid bugs through references to the same object. Besides, the layer thicknesses are extracted and stored internally in a separate list which is used exclusively over the object stored thicknesses. The first and the last given layer are assumed to embed the remaining layers, so that their thickness defined in the `Layer` object has no meaning. Thus the thicknesses of first and last layer are set to 0 the constructor of `Reflector` for convenience in the simulation functions. The thickness configuration can be changed with `setThicknesses()` and a full text representation of the current configuration can be generated with `info()`.

3.1.1 Algorithms and their Scope of Application

There are four methods implemented to calculate the transmittivity function $\mathcal{T}_i(\omega, \theta)$ differing in numerical stability and speed. Those are `TransferMethod()` and `TransferMethodMP()`, which implement the Transfer Matrix Method and on the other side `LSEMethod()` and `SingleLSEMethod()`, which implement the described LSE method. All of those methods take the same kind of parameters, which are frequency ω , incident angle θ and the coefficient vector of the initial wave \underline{t}_0 . The returned values are the transmission and reflection coefficients \underline{t}_N and \underline{r}_0 as well as transmittivity \mathcal{T} and reflectivity \mathcal{R} . The last two quantities are evaluated by calling `Reflector.Intensities()` in turn relies on the layer specific intensities from `Layer.Intensity()`. It should be noted that the implementation also considers that modes with complex wave vector \underline{k} should not contribute to the output intensity. This is implemented as additional factor $|e^{i|\underline{k}|d}|$ with an arbitrary but high d in `Layer.Intensity()`.

To explain the coexistence of the methods, it is helpful to describe and analyse them in the order of their development. The challenge here was not only to get a working implementation, but an implementation that is able to produce valid results in convenient time for the problem described in the introduction.

One important tool for validating the obtained transmittivity values is the sanity check. Each of these methods is checked for energy conservation by evaluating the validity of $\mathcal{R} + \mathcal{T} = 1$, the sum of reflectivity \mathcal{R} and transmittivity \mathcal{T} which was discussed in section 2.3.2. It offers a fast test for reasonable results. However, it can not exclude all kinds of errors so that additional validation against known cases will be provided.

The first attempt was `TransferMethod()`. The TMM offers the most promising properties with regard to computation time for large systems, because existing matrix multiplication algorithms as implemented in the `numpy` package can be used and the addition of layers to the problem only increases the computation time linearly. The latter becomes apparent when considering equation 2.64.

Although the implemented algorithm is fast as expected and is able to pass the sanity check, a significant limitation occurs for layer structures with more than 6 interfaces and frequencies over a few GHz. The sanity of the values of such configurations begins to decay for large angles. Large regions in angle frequency space establish, where the resulting values are covered by a strong noise leading to values of almost diverging magnitude. Examples of that behaviour are shown in the appendix. In extreme cases this leads to ill conditioning of $\underline{\underline{R}}$ from equation 2.66 so that it is not invertible anymore.

It is assumed that this is caused during calculation of very large and very small values with limited precision. This especially occurs in the propagation matrix $\underline{\underline{P}}_n$ from equation 2.61, which is responsible for the propagation of the coefficients through a layer. It contains both exponentially large and small values in the case of evanescent waves. The wave vector adopts a negative complex part so that the lower diagonal entries increase exponentially with layer thickness while the upper diagonal entries decrease with layer thickness.

The effect of the nature of $\underline{\underline{P}}$ was investigated by analysing the continuity in θ of matrix entries with a debugging tool. It was found that the mere composition to the complete transfer matrix $\underline{\underline{S}}$ is less relevant for that effect than the final calculation of the coefficients in equations 2.66 and 2.67. Unfortunately, these are essential to the Transfer Matrix Method.

As other explanations over the source of the numerical instabilities could not be verified and after several unsuccessful attempts of improving numerical stability, the LSE method was considered. It represents the rather heuristic approach to solve the system of equations in one step. The benefit is that the exponentials with magnifying exponent can be reformulated as attenuating exponential functions. Therefore, the numerical issues could be improved in a manner that the required computations can be undertaken successfully.

However, this method has other disadvantages. Firstly, the time complexity is no longer linear in the number of layers. The method is significantly slower for small problems which makes large problems much more time consuming than with the TMM. Another limitation is given by the `numpy` focused coding style, where python loops are avoided by initialising arrays and exploiting faster matrix operations. Here the loop over arrays of initial angles θ and the related frequencies ω was implemented by stacking the matrices and vectors for a single value pair along additional dimensions. As a result, the computation transmittivity values for several hundreds of frequencies with several hundreds of angles each at one time can require more storage than a typical RAM can offer.

Another approach was to use sparse matrices with the package `sparse` which is compatible with `numpy` and implements much more efficient storage of matrices with many zero valued elements. Although the present matrices fulfil this criterion, the assembly of those matrices from `numpy` dense matrices proved too slow in comparison to the gained speed. This is possibly related to the circumstance that the module wraps the computational methods of `scipy.sparse.linalg` which only uses two-dimensional sparse matrices.

For this reason, the method `SingleLSEMethod()` was created as linearised method using python loops. In each iteration, it passes a single angle and frequency to `LSEMethod()`. For that case it was also optimised by using the sparse system solver `spsolve()` from `scipy.sparse.linalg` which improves the performance further.

As the LSE Method also encounters numerical problems for larger structures (more than 30 layers for angles above 60°) a fourth attempt was made by using the module `mpmath`. It provides types with arbitrary numerical precision. A full implementation of the Transfer Matrix Method with `mpmath` is given by `TransferMethodMP()` and several submethods ending with `MP`. This was done by Tobias Hangleiter in analogy to the existing TMM implementation. The `mpmath` approach is able to deliver numerically stable results as expected. However, the computation time is significantly higher than for all other methods, so that it is only used in cases, where the other methods fail.

The advantage of `mpmath` can be also used to improve `SingleLSEMethod()`. If the parameter `optimizing` is enabled, the method switches to `TransferMP()` if the values are not sane.

In addition, another optimisation can be implemented. All these algorithms rely on several subroutines like for example `Layer.getConditionMatrix()`, which calculates the matrix $\underline{\underline{M}}_n$ from equation 2.63. In this and other cases, the function is called several times with the same arguments due to the fact that the

propagating angles in each Layer are equal in each Layer of the same type. For this reason, the results of these subroutines are cached.

Conventional caching decorators require the function parameters to be hashable, but this does not apply for `numpy` arrays. For that reason, caching was implemented by hand. The essential part of this are the hash function `Hash()` which converts an arbitrary number of parameters to a hashable tuple. This hash is then used as key in a dictionary for the results of the hashed function. For each cached function there is such a dictionary stored in either `Reflector` or `Layer`.

In further development, this method may cause errors, if, for example, a new parameters are introduced in `Reflector` or `Layer` that influence the calculation. If such a parameter is changed during runtime, the results of the algorithm may not change at all or change so that the sanity check is not fulfilled anymore. In such a case, this parameter could also be provided to `Hash()` to create new dictionary entries in case it changes.

A different, maybe preferred solution would be to develop or use a more sophisticated caching method that is more stable to such cases.

3.1.2 *Plots and Scripts for Evaluation*

In order to evaluate the total heat transfer, these methods are used to calculate an array of transmittivities over all angles $\theta \in [0^\circ, 90^\circ]$ and over all frequencies $\omega \in (0\text{s}^{-1}, 30 \cdot 10^{11}\text{s}^{-1}]$. The integral 1.1 is then evaluated first by integrating over the angles which is done by `Reflector.spectralTransmission()` using the method `numpy.trapz()`. The weighting factor $\cos\theta$ is also considered so that the resulting values represent spectral transmittivity in z-direction. The total heat flow is calculated with `transmittedPower()` by evaluating the described integrant at the same frequencies as the spectral transmittivity and integrating it analogously to the angles. Also, $\Delta P = \frac{P_t}{P_{in}}$ with transmitted heat flow $P_t = J_z$ and incoming heat flow P_{in} is calculated, which gives a simple measure of the reflectors' efficiency.

The intermediate results of this calculation may be of interest as well. For this purpose, `plotfunctions.py` provides a number of plot functions and scripts that were also used to generate the plots in the later course of this thesis. The first important plot function is `plotAngularTransmission()`. It produces three subplots. In the first, the absolute values of the reflection coefficients are shown which represent the reflected amplitudes. The plot below does the same for the transmission coefficients. In the lowermost plot the resulting transmittivity and reflectivity are shown as functions of incident angle for a fixed frequency. Also

their sum is displayed as proof of correctness of the values. This can be viewed for example in figure 4.2.

In comparison to that, `plotOverview()` accepts transmittivity values from a region in angle-frequency space as two-dimensional array and is able to provide a three-part plot as in figure 4.5. Here the upper left field represents a color plot of the sanity of the transmittivity over frequency and angle axis. Dots coded as 1 denote that the transmittivity at the corresponding angle and frequency was calculated correctly. At the right, the transmittivity values are represented directly in a similar plot. Those two plots help to understand the regions of numerical instabilities but also the behaviour of transparent regions of the reflector under angle or frequency variation. The lower plot, the spectral radiance transmitted through the reflector in comparison to the incident radiance. A textbox also shows the results of the integration over those curves and the ratio of transmitted power. For each plot a boolean parameter is passed to the function to enable or disable the appearance of each plot in the output.

These plot functions also exist in form of a script like function that generates the necessary transmission values by itself and directly provide the output as plot.

In addition to these evaluation plots, there is an additional utility function called `EffectivityOverThickness()`. It is an attempt to automatise the optimisation process that will be described later. The method calculates the ratio of transmitted power as in `transmittedPower()` for a reflector with two different materials with repeating thicknesses. The output is a matrix, where thickness of layer 1 varies along the first axis and the thickness of layer 2 varies along the second axis. This matrix is again represented as colorplot. This plot was not used here as it is very time consuming to compute and has only limited significance.

All described plots can be generated from `fullCalculation.py`. A step by step calculation is also presented. More analysis focused code is presented in the python notebooks `verifications.ipynb` and `dbr_search.ipynb`.

SIMULATIONS

This chapter will present arguments for the validity of the results that can be calculated with the implemented methods. At the same time the properties of some setups are presented. All plots related to verification are generated in the python notebook `verifications.ipynb`.

4.1 SCATTERING AT A SINGLE INTERFACE

In the most simple configuration, a single interface occurs at the boundary of the two half spaces above and below the xy-plane. The calculations for a transition from Copper to Silicon is shown in figure 4.2 and figure 4.1 in the appendix. In the case of transversal horizontal polarisation, the analytical solution from equation 2.43 yields the exact same results, as direct comparison of the calculated values shows. For the other modes, no explicit analytical solutions were found. However, the fulfilled sanity check for all results gives a good argument for their validity.

Additionally, the behaviour of the transmittivity at the critical angles for total reflection can be considered. Recalling that these mark the angles at which a resulting mode changes to evanescent wave propagaion, we can calculate critical angles for all possible transitions between incoming and outgoing modes. These depend only on longitudinal and transversal velocities so that the angles for all reasonable combinations are shown in table 4.1. The critical angles for TH polarised waves are a subset of the critical angles of the shown angles for L an TV polarised waves.

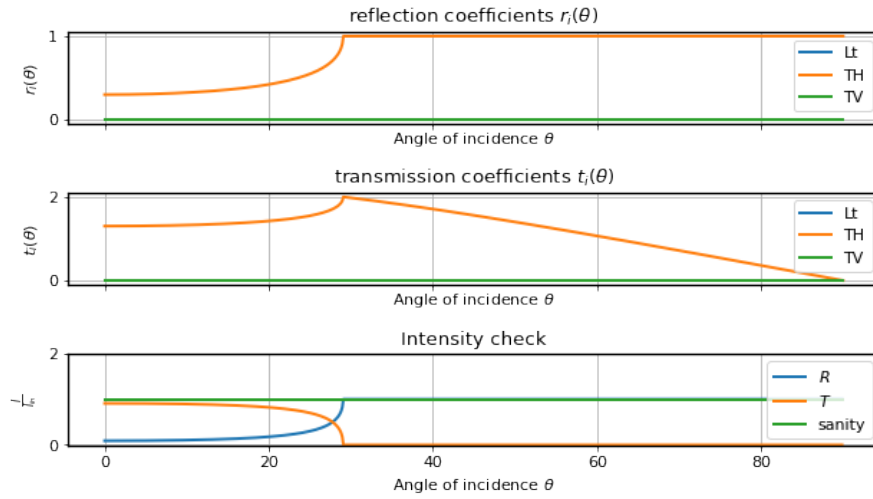
Comparing the obtained angles with the plots, we can see that these can explain the kinks in the funtionality of reflectivity and transmittivity. For example, in case of a longitudinal incident wave, the critical angle denotes the total reflection at the transmitted TV mode. Despite this, the transmitted intensity does not drop completely to zero as the transmitted longitudinal wave can still transport energy.

4.2 MULTILAYER STRUCTURES

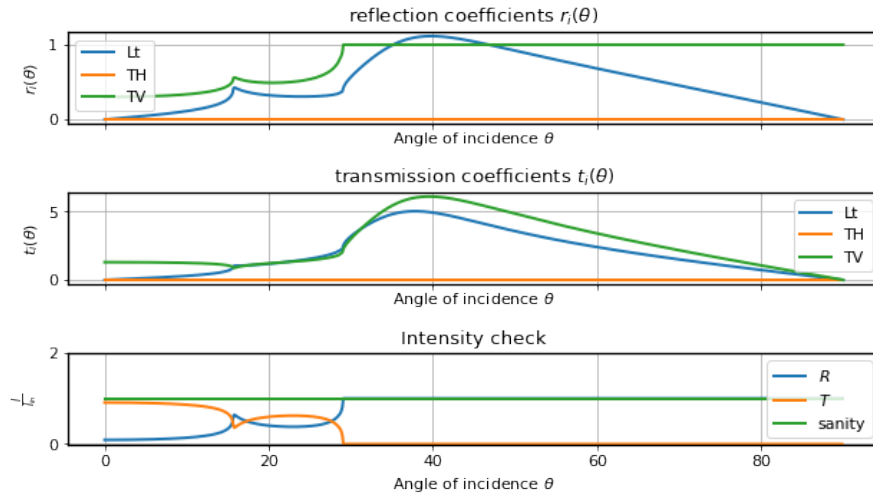
Here an example multilayer structure is presented. According to [20] multilayer structures consisting of low impedance SiO_2 and high impedance metals like

	$c_{L,Cu}$	$c_{T,Cu}$	$c_{L,Si}$	$c_{T,Si}$
$c_{L,Cu}$	90°	-	34.42°	-
$c_{T,Cu}$	28.62°	90°	15.71°	29.06°

Table 4.1: Critical angles for transition from Copper to Silicon depending on velocity of the incoming mode (rows) and outgoing mode (columns)



(a) Scattering of TH polarised waves at a single interface



(b) Scattering of TV polarised waves at a single interface

Figure 4.1

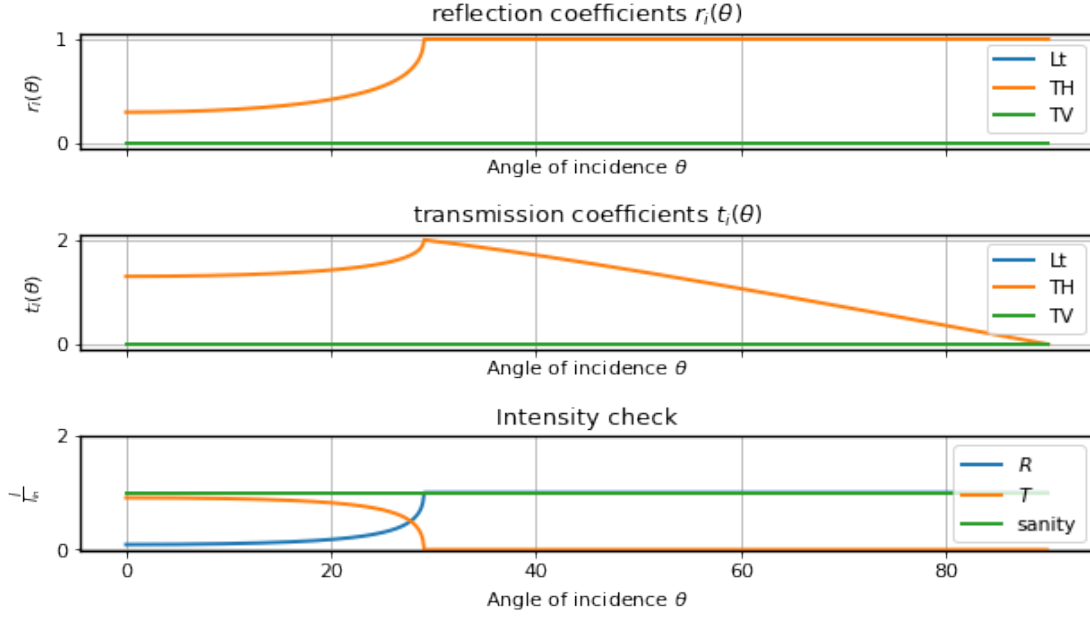


Figure 4.2: Scattering of L polarised waves at a single interface

tungsten or molybdenum are suitable for fabrication of acoustic resonators. For that reason the following plots present simulation result of bragg reflector with a unit cell of SiO_2 and Mo which is repeated eight times and with an embedding layer of SiO_2 . The thicknesses are chosen to be a quarter wavelength of a wave with frequency $f_0 = 100\text{GHz}$ with longitudinal polarisation. With longitudinal velocity $c_{L,\text{SiO}_2} = 8478 \frac{\text{m}}{\text{s}}$ and transversal velocity $c_{T,\text{SiO}_2} = 4725 \frac{\text{m}}{\text{s}}$ of SiO_2 and velocities $c_{L,W} = 5160 \frac{\text{m}}{\text{s}}$ and $c_{T,W} = 2843 \frac{\text{m}}{\text{s}}$ of tungsten these thicknesses are $d_1 = 13.98\text{nm}$ for SiO_2 and $d_2 = 19.16\text{nm}$ for tungsten. The overview plots for calculations with all angles are shown in figures 4.3 to 4.5 for each mode. The positions of the bandgap at f_0 is clearly visible in the longitudinal case and it appears that only uneven orders from equation 2.74 are visible under normal incidence, because of the construction with layers of quarter wavelength thickness. This changes for larger angles where the phase shift per layer becomes dependent on the incident angle and mode. In `verifications.ipynb`, also the case of normal incidence can be examined and the positions of the bandgaps can be compared to the theoretical expectations from section 2.3.4.

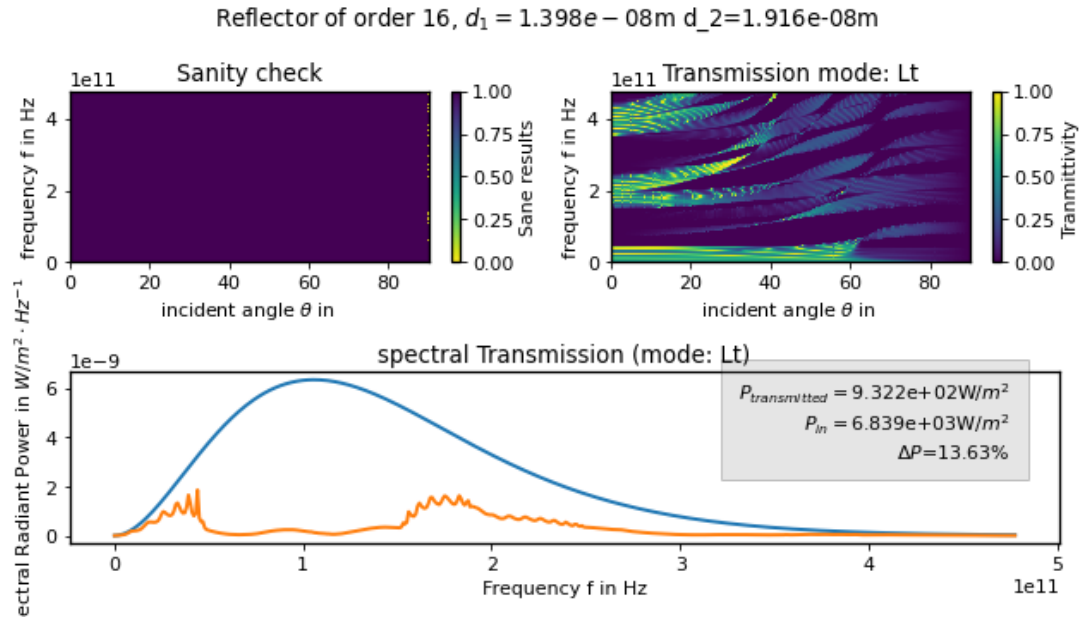


Figure 4.3: Scattering of L polarised waves at a single interface calculated with LSE Method

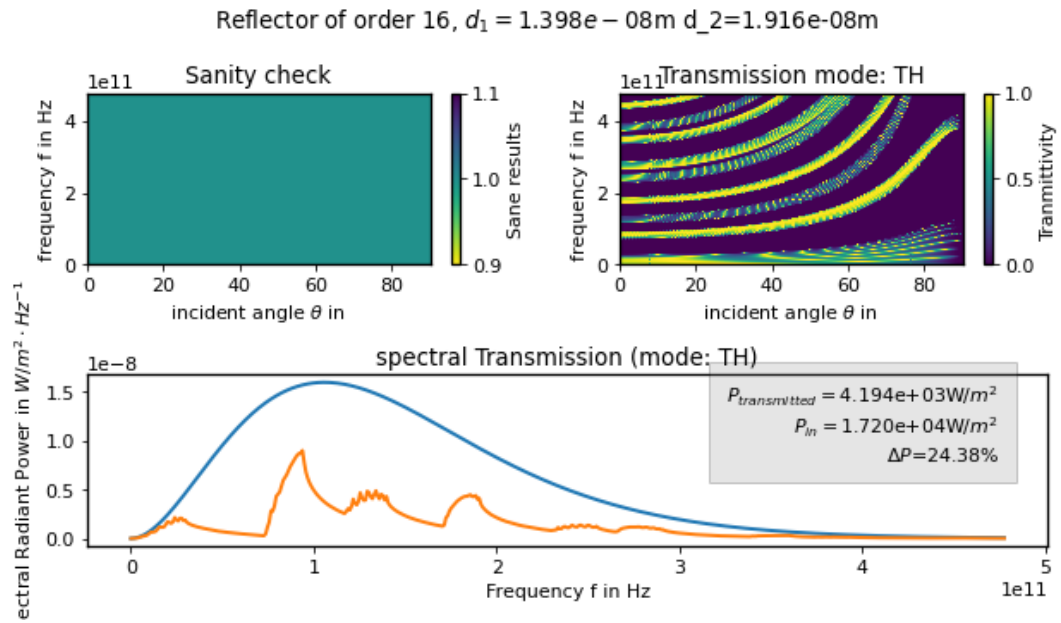


Figure 4.4: Scattering of TH polarised waves at a single interface calculated with LSE Method

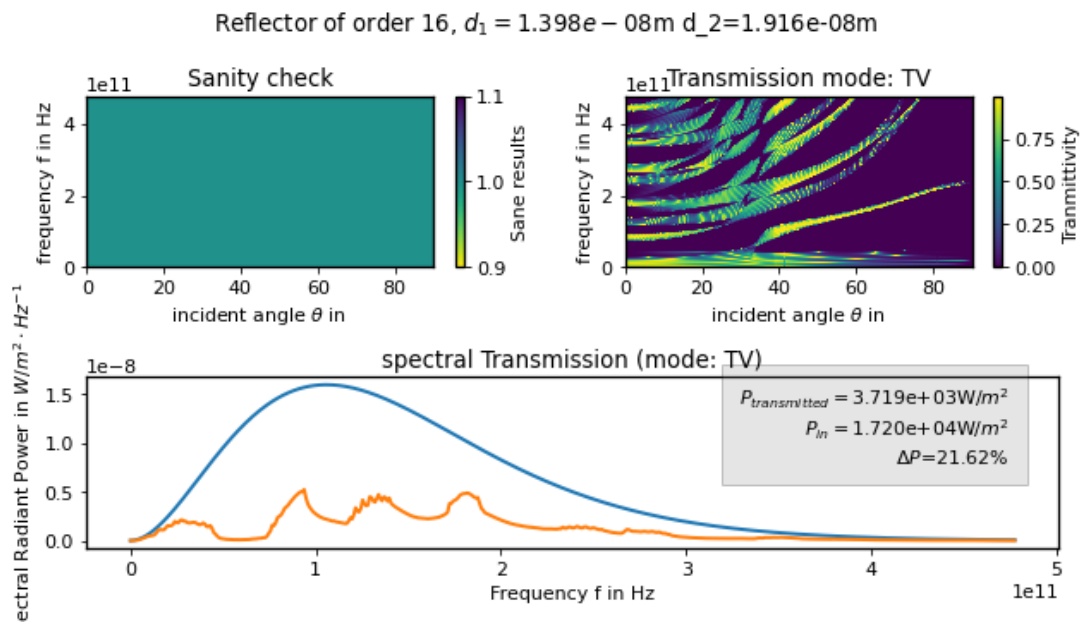


Figure 4.5: Scattering of TV polarised waves at a single interface calculated with LSE Method

CONCLUSION

To conclude, a working simulation framework could be developed. In the course of development, the numerical issues previously encountered by Miles could be mostly removed and the functionality of the calculation over all angles was established. Several kinds of validation, like the check for energy conservation or relations at a single interface reason confidence in the correctness of all not directly verified computations. Also, the sanity check shows to be very capable of detecting numerical instabilities without larger effort.

Although these capabilities are enough to fully calculate larger systems, `TransferMethodMP()` is multiple times slower than `SingleLSEMethod()` so that it may be of interest to optimise the methods calculating the transmission. One way could be, to take advantage of packages like `numba` that are able to speed up python code. In that case, it is necessary to reimplement the optimised method without usage of custom functions or objects except for `numpy` types as these can not be handled by `numba`.

In the future, this simulation can be used to develop a structure that is able to decrease the total expected heat flux to few mW. The theoretical foundations for a systematical search were given in this work. One could think about using the knowledge of the behaviour of the spectral bandgaps for normal incidence to stack several reflectors to a fully reflecting structure. If this can be achieved for normal incidence, the intensity for incident waves for higher angles will be reflected at high rates as well. However, to obtain certainty it must be validated by simulation.

The selection of the right materials will also be a relevant question, which can be also conducted by the given knowledge for the reflection at single interfaces. Some of those ideas are also regarded in the Jupyter notebook `dbr_search.ipynb`

Ultimately, one can fabricate such a structure and then measure its thermal conductance to verify the expectations. In that setting it would be of interest to investigate the influence of surface roughness of the interfaces on the coherence of the phonons. The possibility of surface roughness could also be implemented into the existing model in a future work by following the generalised transfer matrix method presented in [21].

BIBLIOGRAPHY

- ¹E. Leonard, M. A. Beck, J. Nelson, B. Christensen, T. Thorbeck, C. Howington, A. Opremcak, I. Pechenezhskiy, K. Dodge, N. Dupuis, M. Hutchings, J. Ku, F. Schlenker, J. Suttle, C. Wilen, S. Zhu, M. Vavilov, B. Plourde, and R. McDermott, “Digital coherent control of a superconducting qubit”, **Physical Review Applied** **11**, 014009 (2019).
- ²A. Crippa, R. Ezzouch, A. Aprá, A. Amisse, R. Laviéville, L. Hutin, B. Bertrand, M. Vinet, M. Urdampilleta, T. Meunier, M. Sanquer, X. Jehl, R. Maurand, and S. D. Franceschi, “Gate-reflectometry dispersive readout and coherent control of a spin qubit in silicon”, **Nature Communications** **2019 10:1** **10**, 1–6 (2019).
- ³F. Arute, K. Arya, R. Babbush, D. Bacon, and J. C. Bardin, “Quantum supremacy using a programmable superconducting processor”, **Nature** **574**, 505 (2019).
- ⁴J. I. Cirac and P. Zoller, *A scalable quantum computer with ions in an array of microtraps* (2000).
- ⁵T. Brecht, W. Pfaff, C. Wang, Y. Chu, L. Frunzio, M. H. Devoret, and R. J. Schoelkopf, “Perspective open multilayer microwave integrated quantum circuits for scalable quantum computing”, **Nature Publishing Group** **2**, 10.1038/npjqi.2016.2 (2016).
- ⁶H. Bluhm and L. R. Schreiber, “Semiconductor spin qubits - a scalable platform for quantum computing?”, **Proceedings - IEEE International Symposium on Circuits and Systems** **2019-May**, 10.1109/ISCAS.2019.8702477 (2019).
- ⁷L. Lao, B. van Wee, I. Ashraf, J. van Someren, N. Khammassi, K. Bertels, and C. G. Almudever, “Mapping of lattice surgery-based quantum circuits on surface code architectures”, **Quantum Science and Technology** **4**, 10.1088/2058-9565/aadd1a (2018).
- ⁸E. Ferraro, M. Fanciulli, and M. D. Michielis, “Phonon-induced relaxation and decoherence times of the hybrid qubit in silicon quantum dots”, **Physical Review B** **100**, 035310 (2019).
- ⁹M. N. Luckyanova, J. Garg, K. Esfarjani, A. Jandl, M. T. Bulsara, A. J. Schmidt, A. J. Minnich, S. Chen, M. S. Dresselhaus, Z. Ren, E. A. Fitzgerald, and G. Chen, “Coherent phonon heat conduction in superlattices”, **Science** **338**, 936–939 (2012).

- ¹⁰R. Gross and A. Marx, *Festkörperphysik* (De Gruyter Oldenbourg, 2014), pp. 143–155.
- ¹¹S. Simon, *The oxford solid state basics* (Oxford University Press, 2016), p. 290.
- ¹²T. Kundu, *Ultrasonic and electromagnetic nde for structure and material characterization: engineering and biomedical applications* (Taylor & Francis, 2012), pp. 27–30.
- ¹³A. Bedford and D. Drumheller, *Introduction to elastic wave propagation* (Jan. 1994), p. 43.
- ¹⁴J. Achenbach, N.-H. P. Company, and A. E. P. Company, *Wave propagation in elastic solids*, Applied Mathematics and Mechanics Series (North-Holland Publishing Company, 1973).
- ¹⁵L. Brekhovskikh, *Waves in layered media* (Elsevier Science, 2012).
- ¹⁶W. Ewing, *Elastic waves in layered media [by] w. maurice ewing, wenceslas s. jardetzky [and] frank press*, Contribution (McGraw-Hill, 1957), p. 28.
- ¹⁷S. I. Fomenko, M. V. Golub, C. Zhang, T. Q. Bui, and Y. S. Wang, “In-plane elastic wave propagation and band-gaps in layered functionally graded phononic crystals”, *International Journal of Solids and Structures* **51**, 2491–2503 (2014).
- ¹⁸B. Osting, “Bragg structure and the first spectral gap”, *Applied Mathematics Letters* **25**, 1926–1930 (2012).
- ¹⁹G. N. Aliev, B. Goller, D. Kovalev, and P. A. Snow, “Hypersonic acoustic mirrors and microcavities in porous silicon”, *Applied Physics Letters* **96**, 10.1063/1.3367747 (2010).
- ²⁰Y. Satoh, T. Nishihara, T. Yokoyama, M. Ueda, and T. Miyashita, *Development of piezoelectric thin film resonator and its impact on future wireless communication systems*, May 2005.
- ²¹C. C. Katsidis and D. I. Siapkas, “General transfer-matrix method for optical multilayer systems with coherent, partially coherent, and incoherent interference”, *Applied Optics*, Vol. 41, Issue 19, pp. 3978-3987 **41**, 3978–3987 (2002).
- ²²*Nsm archive - physical properties of semiconductors*.
- ²³B. El-Kareh, “Thermal oxidation and nitridation”, *Fundamentals of Semiconductor Processing Technology*, 39–85 (1995).
- ²⁴*Azom materials database*, accessible at <https://www.azom.com/>.

APPENDIX

A.1 CONCRETE FORM OF THE CONDITION MATRICES

In this section the construction of the condition matrices $\underline{\underline{M}}_n$ from equation 2.59 is considered in more detail. With the general wave solution equation 2.53 the strain in layer n tensor evaluates to

$$\begin{aligned} \epsilon_{ij} &= \frac{i}{2} \left((\hat{\mathbf{e}}_i \cdot \underline{\mathbf{u}}(\underline{\mathbf{x}}, t)) (\hat{\mathbf{e}}_j \cdot \underline{\mathbf{k}}_n^t) + (\hat{\mathbf{e}}_j \cdot \underline{\mathbf{u}}(\underline{\mathbf{x}}, t)) (\hat{\mathbf{e}}_i \cdot \underline{\mathbf{k}}_n^t) \right) \\ &= \frac{i}{2} \sum_{p \in \{L, TH, TV\}} t_p \epsilon_{ij,p}^t e^{i(\underline{\mathbf{k}}_p^t \underline{\mathbf{x}} - \omega t)} + r_p \epsilon_{ij,p}^r e^{i(\underline{\mathbf{k}}_p^r \underline{\mathbf{x}} - \omega t)} \end{aligned} \quad (\text{A.1})$$

with

$$\epsilon_{ij,p}^t = \frac{i}{2} \left((\hat{\mathbf{e}}_i \cdot \underline{\mathbf{p}}_p^t) (\hat{\mathbf{e}}_j \cdot \underline{\mathbf{k}}_p^t) + (\hat{\mathbf{e}}_j \cdot \underline{\mathbf{p}}_p^t) (\hat{\mathbf{e}}_i \cdot \underline{\mathbf{k}}_p^t) \right) \quad (\text{A.2})$$

and analogously for $\epsilon_{ij,p}^r$. The condition matrix is then constructed as

$$\underline{\underline{M}} = \begin{pmatrix} \begin{array}{c} | \\ \underline{\mathbf{p}}_L^t \\ | \end{array} & \begin{array}{c} | \\ \underline{\mathbf{p}}_{TH}^t \\ | \end{array} & \begin{array}{c} | \\ \underline{\mathbf{p}}_{TV}^t \\ | \end{array} & \begin{array}{c} | \\ \underline{\mathbf{p}}_L^r \\ | \end{array} & \begin{array}{c} | \\ \underline{\mathbf{p}}_{TH}^r \\ | \end{array} & \begin{array}{c} | \\ \underline{\mathbf{p}}_{TV}^r \\ | \end{array} \\ C_{55} \epsilon_{13,L}^t & C_{55} \epsilon_{13,TH}^t & C_{55} \epsilon_{13,TV}^t & C_{55} \epsilon_{13,L}^r & C_{55} \epsilon_{13,TH}^r & C_{55} \epsilon_{13,TV}^r \\ C_{44} \epsilon_{23,L}^t & C_{44} \epsilon_{23,TH}^t & C_{44} \epsilon_{23,TV}^t & C_{44} \epsilon_{23,L}^r & C_{44} \epsilon_{23,TH}^r & C_{44} \epsilon_{23,TV}^r \\ C_{3i} \epsilon_{ii,L}^t & C_{3i} \epsilon_{ii,TH}^t & C_{3i} \epsilon_{ii,TV}^t & C_{3i} \epsilon_{ii,L}^r & C_{3i} \epsilon_{ii,TH}^r & C_{3i} \epsilon_{ii,TV}^r \end{pmatrix} \quad (\text{A.3})$$

with Einstein convention implied in the last row, in order to fulfill equation 2.59.

A.2 DETAILED PLOTS PICTURING SCOPES OF NUMERICAL INSTABILITES

The following plots show the reflector from section 4.2 calculated with `TransferMethod()` in comparison to the plots from above with `singleLSEMethod()`.

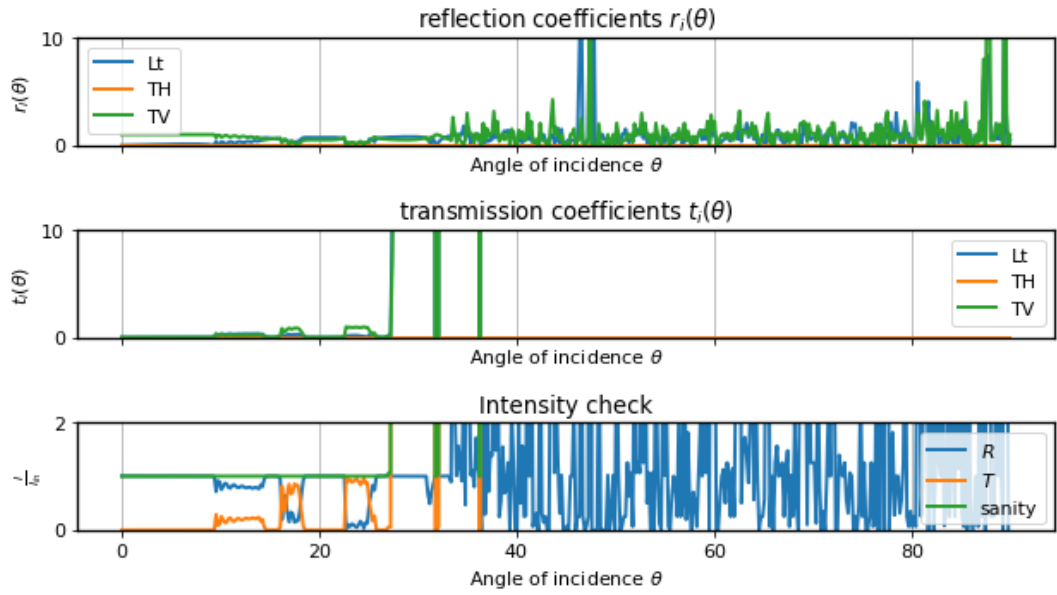


Figure A.1: Angular Plot with frequency $f = 477\text{GHz}$ for TV mode with `TransferMethod()`

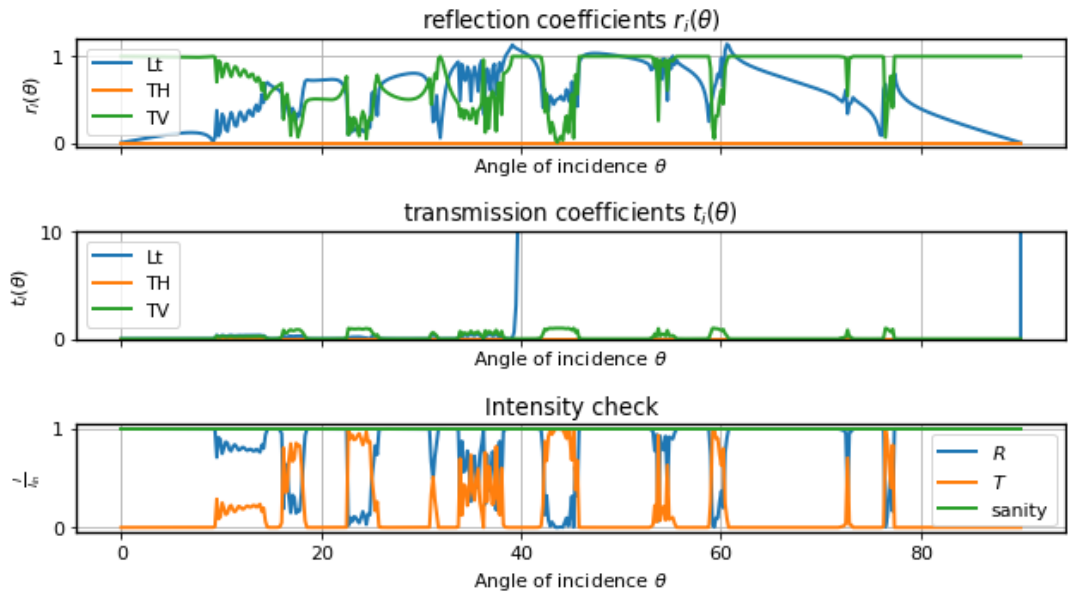
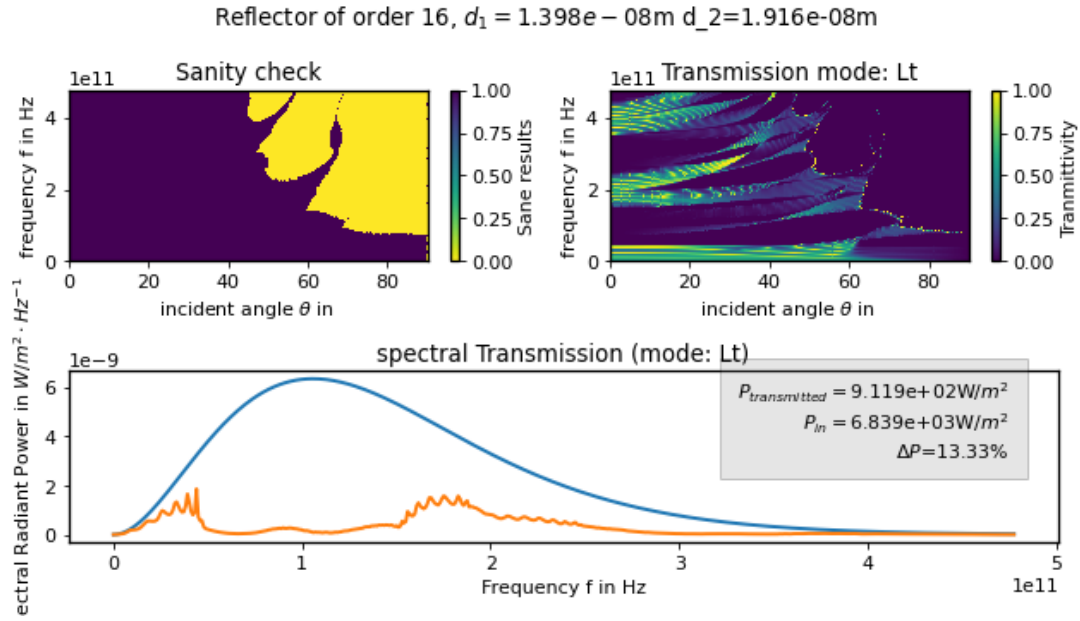
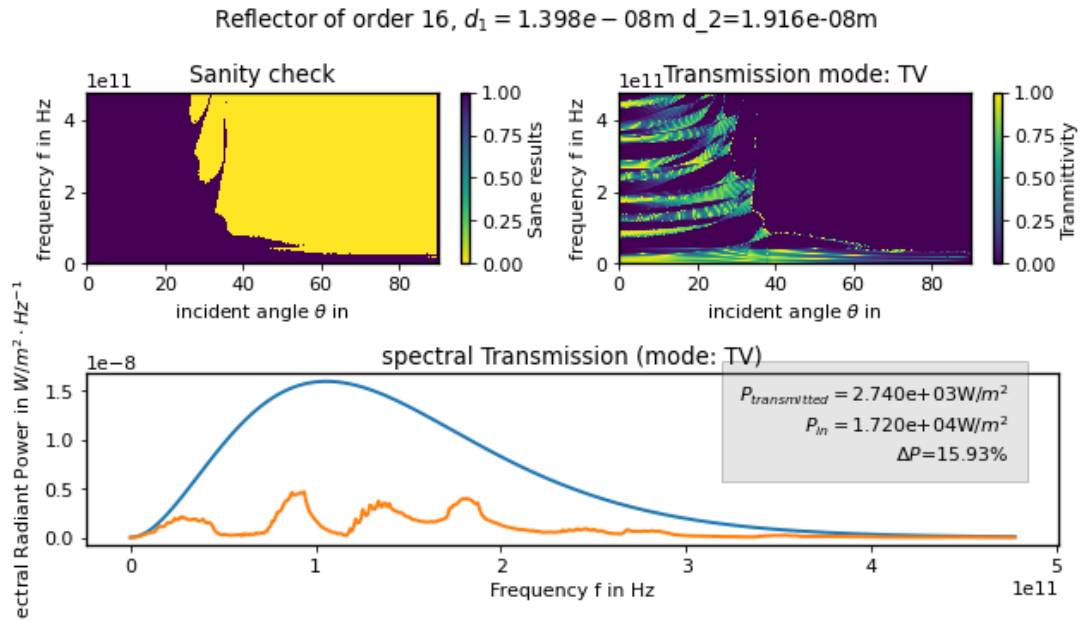


Figure A.2: Angular Plot with frequency $f = 477\text{GHz}$ for TV mode with `singleLSEMethod()`

Figure A.3: Overview for `TransferMethod()` and mode LFigure A.4: Overview for `TransferMethod()` and mode TV

A.3 MATERIALS IN `MATERIALS.PY`

material	density ρ in $\frac{\text{kg}}{\text{m}^3}$	c_L in $\frac{\text{m}}{\text{s}}$	c_T in $\frac{\text{m}}{\text{s}}$	Z_L in $10^7 \frac{\text{Pa s}}{\text{m}}$	Z_T in $10^7 \frac{\text{Pa s}}{\text{m}}$
GaAs [22]	5317	4732	2485	2.516	1.322
Si [22]	2329	8476	4725	1.974	1.100
Si _{0.7} Ge _{0.3} [22]	3332	6814	3785	2.271	1.261
AlGaAs _{0.3} [22]	4852	4957	2577	2.405	1.251
SiO ₂ [23]	2270	5590	3524	1.269	0.800
Ge [22]	5323	5366	2775	257	177
Cu [24]	8920	4791	2295	4.274	2.048
Sn [24]	5765	3290	1645	1.897	0.948
W [24]	19300	5160	2843	9.959	5.487
Mo [24]	10220	7662	3426	7.831	3.502

Table A.1: Table of materials in `materials.py` with velocities c and impedances Z for longitudinal and transversal polarisations

STATEMENT OF AUTHORSHIP

I hereby declare that I completed this thesis on my own and that information which has been directly or indirectly taken from other sources has been noted as such. Neither this nor a similar work has been presented to an examination committee.

Aachen, September 8, 2021

.....

Sebastian Kock